

Send Less, Perceive More: Masked Quantized Point Cloud Communication for Loss-Tolerant Collaborative Perception

Sheng Xu¹, Enshu Wang^{1,*}, Hongfei Xue^{2,*}, Jian Teng³, Bingyi Liu³,
Yi Zhu⁴, Pu Wang², Libing Wu¹, Chunming Qiao⁵

¹School of Cyber Science and Engineering, Wuhan University,

²University of North Carolina at Charlotte,

³Wuhan University Of Technology,

⁴Wayne State University,

⁵University at Buffalo

{xusheng02, wanges17, wu}@whu.edu.cn, {hongfei.xue, Pu.Wang}@charlotte.edu,
{tengjian, byliu}@whut.edu.cn, yzhu39@wayne.edu, qiao@buffalo.edu

*Corresponding authors.

Abstract

Collaborative perception allows connected vehicles to overcome occlusions and limited viewpoints by sharing sensory information. However, existing approaches struggle to achieve high accuracy under strict bandwidth constraints and remain highly vulnerable to random transmission packet loss. We introduce *QPoint2Comm*, a quantized point-cloud communication framework that dramatically reduces bandwidth while preserving high-fidelity 3D information. Instead of transmitting intermediate features, *QPoint2Comm* directly communicates quantized point-cloud indices using a shared codebook, enabling efficient reconstruction with lower bandwidth than feature-based methods. To ensure robustness to possible communication packet loss, we employ a masked training strategy that simulates random packet loss, allowing the model to maintain strong performance even under severe transmission failures. In addition, a cascade attention fusion module is proposed to enhance multi-vehicle information integration. Extensive experiments on both simulated and real-world datasets demonstrate that *QPoint2Comm* sets a new state of the art in accuracy, communication efficiency, and resilience to packet loss.

1. Introduction

Multi-agent collaborative perception has emerged as a critical technology for autonomous driving systems [1, 8, 24, 27, 54]. It enables multiple agents, such as vehicles and roadside units, to exchange sensor data (e.g., camera, Li-

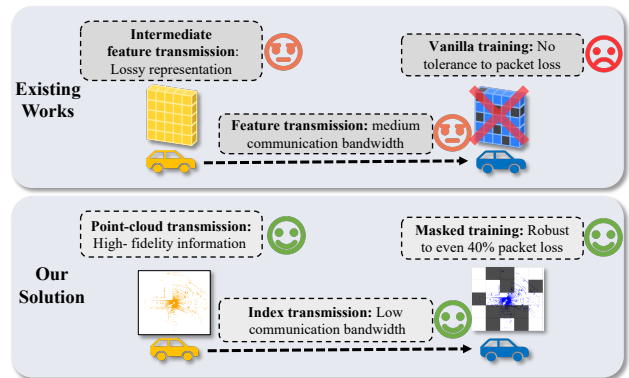


Figure 1. Comparison between our proposed quantized point cloud-based framework and existing feature-based methods for collaborative perception.

DAR) in real time [32, 39, 62], extending each agent’s perceptual field beyond line-of-sight limitations. By sharing information, collaborative perception effectively mitigates occlusion, sparse observations, and restricted viewpoints, resulting in improved accuracy and robustness for 3D object detection [9, 19, 20]. With the rapid advancement of high-precision sensors and low-latency vehicular communication [9, 48], collaborative perception has become a key enabler for long-range perception in connected and collaborative autonomous driving environments [34].

Despite recent progress, practical deployment of collaborative perception still faces major challenges, including limited bandwidth [48], packet loss [2], localization error [32], and transmission delay [10, 19]. To balance the bandwidth constraints and the perception performance, existing methods can be categorized by the format of shared information: (1) Raw-data transmission [7, 60], which

achieves high accuracy but demands excessive bandwidth; (2) Feature-level transmission [19, 26, 31, 51, 52, 58], which reduces bandwidth by sharing encoded features but still suffers from high communication volume and information loss; (3) Result-level transmission [42, 44], which shares only detection results (e.g., bounding boxes), offering high efficiency at the cost of losing contextual cues and increasing noise sensitivity. While these strategies mainly focus on bandwidth reduction, they often overlook communication instability. To address packet loss, recent works either dynamically allocate communication resources [5, 14, 29, 55] or utilize historical frames to infer missing data [18, 41, 46]. However, the former cannot handle random loss typical of real-world networks, and the latter accumulates prediction errors and incurs heavy computational cost and delay. Consequently, existing frameworks still show poor tolerance for packet loss during communication. These limitations underscore two fundamental challenges in collaborative perception: (1) *How to efficiently transmit raw sensor information to preserve high perception performance with minimal bandwidth cost; and* (2) *How to design a lightweight system that maintains strong detection performance and tolerance to communication packet loss?*

To address these challenges, we introduce QPoint2Comm, a collaborative perception framework that delivers high accuracy, low communication cost, and strong robustness to random packet loss. The key idea is to transmit compact discrete indices of the point clouds from LiDAR data, largely reducing communication overhead while preserving raw information for accurate perception. Specifically, (i) we introduce a discrete point cloud representation, which directly quantizes raw LiDAR points into discrete codebook indices. Despite the significantly reduced bandwidth, this is the first approach in collaborative perception to transmit point clouds in a fully discrete form while preserving rich raw information and maintaining high-fidelity 3D perception. (ii) We introduce a masked training strategy in which a lightweight network is trained on randomly masked voxel grids, enabling robust high-fidelity 3D perception under random packet loss and making QPoint2Comm the first packet-loss-tolerant collaborative perception framework. (iii) Unlike conventional direct fusion, our approach first cascades ego features with collaborative inputs before performing pyramid-scale fusion, improving robustness to temporal delays and localization errors. In addition, the incorporation of feature filtering and prediction refinement [19, 30] improves robustness and yields superior detection accuracy. The main contributions of this work are:

- We propose QPoint2comm, the first quantized point cloud framework for collaborative perception. By transmitting compact discrete indices through a shared codebook,

it substantially reduces bandwidth while preserving rich raw geometric information to support high detection accuracy.

- Through masked training, our framework can tolerate random communication packet loss during collaborative perception, sustaining reliable perception even under severe loss.
- We introduce a pyramid-scale with cascade attention fusion strategy, which first cascades ego features with filtered collaborative cues and then performs pyramid-scale fusion, improving performance and robustness.
- Extensive experiments on OPV2V [52] and DAIR-V2X [56] demonstrate that QPoint2comm consistently outperforms state-of-the-art methods, achieving AP@0.7 gains of 4.10% and 5.18%, respectively, while maintaining low bandwidth overhead and stable performance even under high packet loss rates.

2. Related Work

2.1. Collaborative Perception

Collaborative perception aims to enhance the perception capabilities of individual agents by sharing perception information, enabling better detection performance to complex environments. Existing methods can be broadly categorized based on the type of transmitted data. Raw-data transmission directly shares sensor measurements such as LiDAR point clouds, achieving high perception performance but consuming significant bandwidth [7, 59, 60]. For instance, EMP [60] dynamically adjusts the shared point cloud range to improve scalability under varying road conditions; however, directly sharing raw point clouds is impractical due to excessive bandwidth consumption. Feature-level transmission shares encoded spatial features to reduce bandwidth, but still incurs substantial communication costs [19, 26, 31, 43, 51, 58], and performance may degrade due to information loss during encoding. Recent approaches aim to mitigate this by selectively transmitting features, Where2comm [19] uses confidence-based selection. In order to further reduce bandwidth, CodeFilling [21], CoGMP [15], and QCTF [6] employ VQ-VAE [47]-based quantization on already extracted features. Since feature extraction itself compresses the raw point cloud, applying quantization afterward constitutes a second-stage compression, which inevitably leads to additional information loss. Result-level transmission shares only detection outputs, minimizing bandwidth usage, yet is highly sensitive to noise and localization errors [22, 42, 45, 53]. Although mm-Cooper [30] combines multi-stage transmissions, its communication efficiency is unstable, leading to inconsistent performance. To address these limitations, we propose the first collaborative perception framework that quantizes point clouds into discrete indices, employs a mask training

mechanism (achieving low-bandwidth transmission and inherent tolerance to packet loss), and cascades ego features prior to fusion (thereby improving robustness and yielding superior performance compared to prior methods).

2.2. Point Cloud Representation

LiDAR point clouds [16] are a core 3D representation, capturing spatial geometry and distance information. Early methods, such as LiDAR GAN [3], LiDAR VAE [3], and ProjectedGAN [40], synthesize point clouds from partial or low-resolution inputs, but struggle to reconstruct auxiliary attributes like reflectivity or intensity, which are crucial for autonomous driving. Diffusion-based approaches, including R2DM [36], LiDARGen [63], and LiDM [38], generate high-fidelity point clouds but focus on generation rather than faithful reconstruction and require iterative steps, limiting real-time use. Discrete representation methods based on VQ-VAE [47], such as Point-BERT [57] and UltraLiDAR [49], enable compact encoding and efficient reconstruction, but often struggle with sparse LiDAR data or attribute recovery. Motivated by these insights, we propose a discrete LiDAR representation supporting compact encoding, accurate one-step reconstruction, and low-bandwidth transmission, preserving both geometric and reflective information for robust multi-agent collaborative perception under limited bandwidth.

2.3. Packet Loss during Transmission

To address communication unreliability in collaborative perception, several recent studies have focused on mitigating packet loss under limited bandwidth constraints. Some methods, such as RL-based [5] and UAHRL [55], mitigate packet loss by dynamically allocating communication resources. R-ACP [14] and Edge-Assisted [29] address the issue by selectively discarding less important regions of feature maps. PACP [13] alleviates packet loss by discarding redundant features and dynamically compressing critical ones. SmartCooper [61] enhances robustness by adaptively dropping negatively contributing data. However, the above methods struggle to handle the random loss that occurs in real-world collaborative perception scenarios. To overcome this limitation, another line of research explores approaches that can handle random packet loss. Methods such as RCooper [46] and RCP [18] leverage historical frames, but errors accumulate when multiple frames are lost. V2V-CoPer [41] and LCRN [25] use ego information to recover missing regions or enhance detection performance but incur high computational cost. All these methods perform poorly under high packet loss and lack inherent loss tolerance, making them impractical for real-time deployment. In contrast, we propose a lightweight random masking strategy that provides inherent tolerance to real-world random packet loss without relying on historical frames, achieving

robust perception under severe loss with low computational cost.

3. Methodology

3.1. Overview

Conventional collaborative perception methods relying on feature-level sharing face two challenges: preserving rich spatial information with minimal bandwidth, and coping with random packet loss. As shown in Fig. 1, our method transmits compact discrete point cloud indices, retaining more raw information at low bandwidth. With masked training, it achieves robust detection even under 40% packet loss, demonstrating superior resilience and accuracy.

To send less while perceiving more information and to remain robust under packet loss, we propose QPoint2comm, a collaborative perception framework that encodes LiDAR point clouds into compact discrete indices using shared codebooks for communication, and later reconstructs the corresponding point representations on the ego vehicle. The key modules of our framework are as illustrated in Fig. 3. Each agent first employs the DCR Encoder (Sec. 3.2) to encode raw LiDAR data into compact and semantically rich discrete codes via a shared codebook, substantially reducing transmission overhead. On the ego vehicle, the DCR Decoder reconstructs collaborative point clouds from these codes, preserving more details. To handle missing features caused by packet loss during transmission, we fill them using a learnable feature (Sec. 3.3), enabling the model to inherently tolerate incomplete transmissions and maintain robust perception. Both ego features and collaborative features are fed into the Feature Fusion and Bounding Box Generation module (Sec. 3.4), which includes the Pyramid-scale with Cascade Attention Fusion (PCAF) module (Sec. 3.5), producing the final detection results.

3.2. Discrete Point Cloud Representation

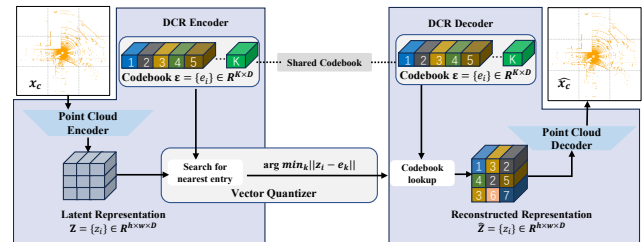


Figure 2. The Discrete Point Cloud Representation (DCR) module is trained to encode point clouds into discrete index sequences and to faithfully reconstruct them via a shared codebook.

As shown in Fig. 2, the Discrete Point Cloud Representation (DCR) module encodes LiDAR point clouds into compact, transmission-efficient discrete codes using shared codebooks, ensuring consistent representation across collaborative and ego agents. Unlike standard VQ-VAE [47],

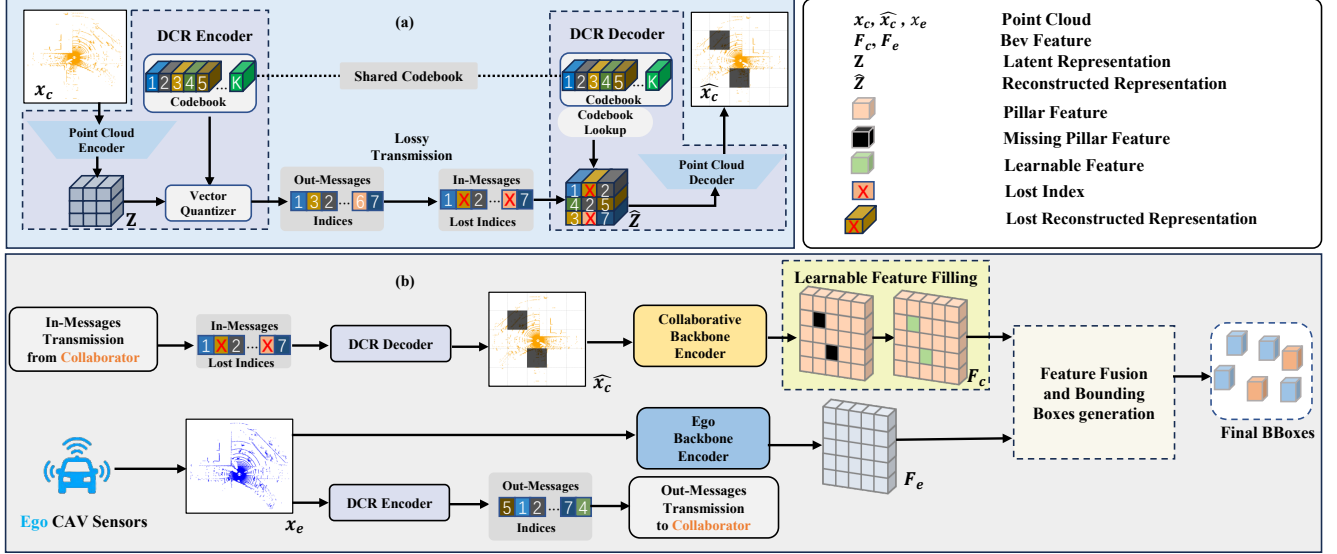


Figure 3. Overview of the proposed collaborative perception framework, consisting of Discrete Point Cloud Representation (Sec. 3.2) for point cloud encoding and decoding, Packet-loss Tolerant Design (Sec. 3.3) to enable communication with missing packets, Feature Fusion and Bounding Boxes Generation (Sec. 3.4) module for generating final bounding boxes.

which struggles with sparse and continuous 4D point cloud distributions (3D coordinates and reflectivity), DCR adopts a one-hot voxel grid strategy. The input point cloud is discretized into a regular 3D voxel grid of size $\mathcal{H} \times \mathcal{W} \times \mathcal{L}$, analogous to 2D pixel grids. To represent both geometry and reflectivity, DCR employs a dual-codebook design:

- a spatial occupancy codebook to model grid-level occupancy patterns;
- an intensity codebook to capture reflectivity characteristics within each voxel grid.

The DCR module is composed of three core components:

- (1) Point Cloud Encoder E :** Given a point cloud x , we first voxelize it into a 3D grid and define an occupancy tensor $X_{\text{occ}} \in \{0, 1\}^{\mathcal{H} \times \mathcal{W} \times \mathcal{L}}$ and an intensity tensor $X_{\text{int}} \in [0, 1]^{\mathcal{H} \times \mathcal{W} \times \mathcal{L}}$. These are passed through corresponding encoders to obtain latent representations: $Z = E(X) \in \mathbb{R}^{h \times w \times D}$.
- (2) Vector Quantization:** Each vector z_i in Z is replaced with the nearest entry in the learnable codebook $\mathcal{E} = \{e_k\}_{k=1}^K$, where $e_k \in \mathbb{R}^D$. The quantized reconstructed representation is denoted as: $\hat{Z} = q(Z) = \{e_{k^*}\}$, where k^* is computed by: $k^* = \arg \min_k \|z_i - e_k\|_2^2$.
- (3) Point Cloud Decoder:** To reconstruct the point cloud, we sample points from Gaussian distributions centered at the grid centroids. The decoder is denoted as: $\hat{X} = \text{Dec}(\hat{Z}; \mathcal{N}(\mu, \sigma^2 I))$, where μ denotes the grid centroid, and σ^2 controls the variance of the Gaussian sampling around the centroid. This stochastic reconstruction enhances robustness by capturing the point distribution within each occupied grid.

Training. The DCR module is trained using the following losses. The quantization losses for the occupancy code-

book $\mathcal{L}_{\text{vq,occ}}$ and the intensity codebook $\mathcal{L}_{\text{vq,int}}$ are both computed as follows: $\mathcal{L}_{\text{vq}} = \|X - \hat{X}\|_2^2 + \|\text{sg}[E(X)] - \hat{Z}\|_2^2 + \|\text{sg}[\hat{Z}] - E(X)\|_2^2$, where $\text{sg}[\cdot]$ denotes the stop-gradient operation [47]. Occupancy Reconstruction Loss is computed using voxel-wise binary cross-entropy: $\mathcal{L}_{\text{occ,reconstruct}} = -\frac{1}{V} \sum_{v=1}^V [y_v \log(\hat{y}_v) + (1 - y_v) \log(1 - \hat{y}_v)]$, where $y_v \in \{0, 1\}$ denotes the ground-truth occupancy label, V is the total grids and \hat{y}_v is the predicted probability. Reflectivity Intensity Loss is computed as mean squared error over all occupied grids: $\mathcal{L}_{\text{int,reconstruct}} = \frac{1}{N_{\text{occ}}} \sum_{v=1}^{N_{\text{occ}}} (\hat{I}_v - I_v^{\text{gt}})^2$, where \hat{I}_v and I_v^{gt} are the predicted and ground-truth normalized intensities, respectively and N_{occ} denotes the number of truly occupied grids.

As shown in Fig. 3 (a), the DCR module enables collaborative agents to transmit compact codebook indices to the ego agent. Ego reconstructs the point cloud via the shared codebooks, allowing low-bandwidth communication while preserving rich information, improving detection accuracy.

3.3. Packet-loss Tolerant Design

Detection Backbone. In multi-agent collaborative perception, let $N = \{1, \dots, n\}$ denote the set of agents. When agent i is the ego vehicle, the remaining $n - 1$ agents transmit their discrete codebook indices and poses. The ego agent reconstructs and transforms the received point clouds into its coordinate frame. Our model uses distinct PointPillar [23] backbones for the ego and collaborators, denoted as ψ_E and ψ_C . The ego feature is encoded into a BEV representation $F_e = \psi_E(x_e) \in \mathbb{R}^{C \times H \times W}$, while each collaborator's feature is $F_c = \psi_C(x_c)$, where x_e and x_c are the

point clouds, and C, H, W are the feature map dimensions. **Mask Training.** At the ego agent, the point clouds received from collaborative agents are processed by the collaborative backbone encoder $\psi_C(\cdot)$ to extract pillar features. To improve robustness against packet loss, a random masking function $\mathcal{M}_r(\cdot)$ is applied on the extracted pillar features during training: $\tilde{F} = \mathcal{M}_r(\psi_C(x_c)) \in \mathbb{R}^{C \times H \times W}$, where \tilde{F} contains randomly masked features. For masked regions, their features are replaced by a learnable feature $f_{\text{learnable}} \in \mathbb{R}^C$, yielding the collaborative feature F_c . This Mask Training design allows the model to tolerate random packet loss in real-world communication, as the learnable feature effectively fills missing pillar features, making the collaborative feature robust to incomplete transmissions.

As shown in Fig. 3 (a) and (b), during inference, some codebook indices may be lost due to environmental fluctuations, leading to missing pillar features. These missing features are replaced with the learnable feature $f_{\text{learnable}}$, producing the collaborative feature F_c . In practice, one codebook index corresponds to multiple voxel grids, the loss of a single codebook index can result in partial occupancy loss across multiple voxel grids. We adopt a strategy where any grid with missing portions is treated as fully lost. Mask Training randomly masks features and fills them with a learnable feature $f_{\text{learnable}}$, enabling inherent tolerance to packet loss and robust perception under high-loss conditions.

3.4. Feature Fusion and Bounding Boxes Generation

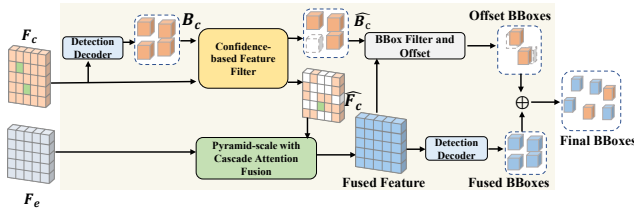


Figure 4. The Feature Fusion and Bounding Boxes generation.

As illustrated in Fig. 4, both collaborative feature F_c and ego feature F_e are fed into the Feature Fusion and Bounding Box Generation module, which produces the final detection results. The key components of this module are as follows: **Confidence-based Feature Filter.** Motivated by the design in Where2comm [19], the Confidence-based Feature Filtering (CFF) module suppresses low-confidence regions. Each F_c is processed by a convolutional network to produce spatial confidence maps $G_f, G_b \in [0, 1]^{H \times W}$. Regions with confidence below the p -th percentile τ_p are filtered, and Gaussian smoothing [33] reduces spatiotemporal noise. The filtered confidence maps are computed as: $\mathbb{I}_{\{G_{f,b} > \tau_p\}} = 1$ if $G_{f,b} > \tau_p$, otherwise 0, $\hat{G}_{f,b} = G_{f,b} \odot \mathbb{I}_{\{G_{f,b} > \tau_p\}} \odot \mathcal{G}_\sigma(G_{f,b})$, and the filtered collaborative fea-

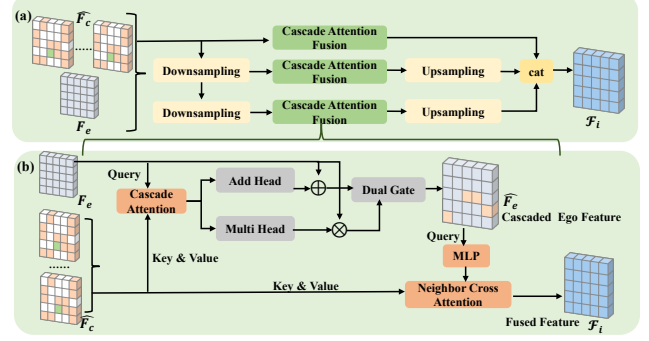


Figure 5. (a) The Pyramid-scale Fusion. (b) The Cascade Attention Fusion (CAF).

tures and bounding boxes are obtained by $\hat{F}_c = \hat{G}_f \otimes F_c$ and $\hat{B}_c = \hat{G}_b \otimes B_c$, where \mathbb{I} denotes the indicator function, $B_c = \text{Detector}(F_c)$ and $\mathcal{G}_\sigma[\cdot]$ is a Gaussian smoothing filter. **Pyramid-scale Fusion with Cascade Attention.** The Pyramid-scale Fusion with Cascade Attention module generates fused features F_i used both to produce the fused bounding boxes and to refine collaborative bounding boxes within the BFO module, which will be elaborated in Sec. 3.5

BBox Filter and Offset. Following the approach of mmCooper [30], the BBox Filter and Offset (BFO) refines collaborative bounding boxes \hat{B}_c . Low-quality boxes are discarded, and remaining boxes are corrected. Offsets are supervised by smooth absolute error \mathcal{L}_{off} [17], and quality scores by focal loss $\mathcal{L}_{\text{score}}$ [28].

3.5. Pyramid-scale Fusion with Cascade Attention

As illustrated in Fig. 5, the Pyramid-scale Cascade Attention Fusion (PCAF) module applies Pyramid-scale Feature Fusion (PFF) to aggregate multi-resolution contextual information. At each scale, Cascade Attention Fusion (CAF) sequentially cascades the ego feature with filtered collaborative features, allowing the ego to incorporate complementary information from other agents, mitigating occlusion and uncertainty, and producing robust fused features for improved detection.

Cascade Attention Fusion (CAF). Within the CAF, the ego features serve as Query while the collaborative features provide Key and Value. The CAF output is split into two augmentation pathways to supplementary and enhancement effects simultaneously:

- (1) Additive path for information supplement, which introduces complementary cues from collaborators: $A_{\text{add}} = H_{\text{add}}(\text{Attn}(F_e, \hat{F}_c, \hat{F}_c)) + F_e$,
- (2) Multiplicative path for information enhancement, which enhances ego representation based on the collaborative cues: $A_{\text{mul}} = H_{\text{mul}}(\text{Attn}(F_e, \hat{F}_c, \hat{F}_c)) \otimes F_e$,

These two paths are then dynamically fused via a learnable gating mechanism to balance information supplement and

information enhancement:

$$\hat{F}_e = \sigma(W_g) \otimes A_{\text{add}} + (1 - \sigma(W_g)) \otimes A_{\text{mul}}, \quad (1)$$

where H_{add} and H_{mul} are projection heads for each path, σ denotes the sigmoid function, and W_g are channel-wise gating weights learned to adaptively control the contribution of each path. This design ensures that the ego features are robustly reinforced before pyramid-scale fusion, leading to more reliable and precise collaborative perception. The PFF fuses cascaded ego features \hat{F}_e with filtered collaborative features \hat{F}_c across pyramid-level using neighbor-cross-attention, followed by upsampling and concatenation to produce the final fused feature \mathcal{F}_i . The CAF module cascades ego features before fusing with pyramid-scale collaborative information, improving robustness and accuracy compared to direct fusion.

3.6. Loss Functions

Training Stage 1: Discrete Point Cloud Representation.

The occupancy and intensity codebooks are trained separately with losses $\mathcal{L}_{\text{occ}} = \mathcal{L}_{\text{vq,occ}} + \mathcal{L}_{\text{occ,reconstruct}}$, $\mathcal{L}_{\text{int}} = \mathcal{L}_{\text{vq,int}} + \mathcal{L}_{\text{int,reconstruct}}$, where $\mathcal{L}_{\text{vq,occ}}$ and $\mathcal{L}_{\text{vq,int}}$ denote the VQ losses for occupancy and intensity codebooks.

Training Stage 2: Object Detection. The detection heads [4] decode the fused features \mathcal{F}_i . The regression head predicts geometric parameters for each anchor box: $\mathcal{O}_{\text{reg}} = f_{\text{dec}}^r(\mathcal{F}_i) \in \mathbb{R}^{7 \times H \times W}$, where the output channels correspond to the center coordinates (x, y, z) , box dimensions (l, w, h) , and yaw angle θ . The classification head produces confidence scores: $\mathcal{O}_{\text{cls}} = f_{\text{dec}}^c(\mathcal{F}_i) \in \mathbb{R}^{2 \times H \times W}$. The overall detection loss is formulated as:

$$\mathcal{L} = \mathcal{L}_{\text{reg}} + \mathcal{L}_{\text{cls}} + \mathcal{L}_{\text{off}} + \mathcal{L}_{\text{score}}, \quad (2)$$

where \mathcal{L}_{reg} denotes the regression loss for geometric parameters, \mathcal{L}_{cls} is the focal loss for classification.

4. Experiments

4.1. Datasets and Experimental Settings

Datasets. OPV2V [52] is a public vehicle-to-vehicle collaborative perception dataset, simulated by OpenCDA [50] and CARLA [11], containing 73 driving scenarios with synchronized LiDAR point clouds and RGB images, and over 11,464 annotated frames encompassing more than 230,000 precise 3D bounding boxes. DAIR-V2X [56] is a large-scale real-world multimodal dataset for 3D object detection, comprising over 71,254 synchronized frames of LiDAR point clouds and camera images.

Evaluation Metrics. We report Average Precision at IoU thresholds [12] of 0.5 and 0.7, following the KITTI [35] benchmark. Communication cost is measured by: $\log_2((2 \times \mathcal{N} \times \log_2 K + 6 \times 32)/8)$, where $\mathcal{N} = h \times w$

Table 1. Collaborative Perception Performance on OPV2V and DAIR-V2X Datasets. Conditions: 100ms Time Delay, 0.2m Localization Error, 0.2° Heading Error. Metric: AP@0.7 / AP@0.5 (↑). Bold = Best, Underline = Second-Best.

Models	OPV2V	DAIR-V2X
	AP@0.7 / AP@0.5	AP@0.7 / AP@0.5
No Fusion [23]	48.66/68.71	43.57/50.03
Late Fusion [23]	59.48/79.62	34.47/51.14
Intermediate Fusion [23]	70.82/88.41	39.38/56.22
When2comm [31]	57.55/74.11	33.68/48.20
DisoNet [26]	68.64/84.72	40.69/52.67
Where2comm [19]	69.73/85.16	43.71/59.52
V2X-ViT [51]	70.06/84.65	40.43/53.08
ERMVP [58]	69.71/86.63	46.96/64.21
SICP [37]	67.13/82.86	41.03/52.72
mmCooper [30]	78.11/88.93	48.27/65.12
Ours	82.21/92.18	53.45/67.97

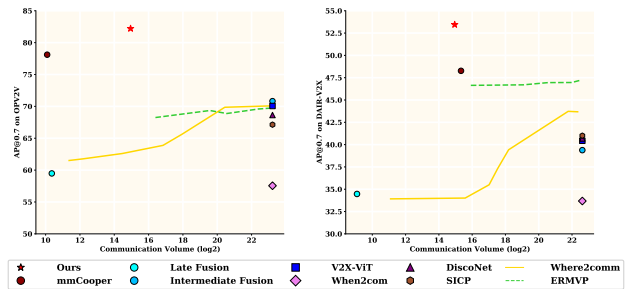


Figure 6. Decton performance and communication volumes of all models on the OPV2V and DAIR-V2X.

is the number of quantized vectors, K is the codebook size, 2 represents dual-coodbook, and 6 represents 6 pose-related parameters (32 bits each), converted to bytes.

Implementation Details. All models are trained on NVIDIA L20 GPUs using a two-stage pipeline. Stage 1 pre-trains DCR with Adam for 160 epochs (batch size 3, codebook size 2,048, vector dimension 1,024). Stage 2 trains a PointPillar [23] backbone for 60 epochs, with batch sizes of 3 on OPV2V and 5 on DAIR-V2X. The mask ratio is 0.3 for both datasets, CFF percentiles p -th are set to 0.35 (OPV2V) and 0.2 (DAIR-V2X), and the codebook is frozen after Stage 1.

4.2. Quantitative Results

Detection Precision. As shown in Tab. 1, under conditions with 100 ms time delay, 0.2 m localization error, and 0.2° heading error, our proposed QPoint2comm consistently outperforms all baselines (When2com [31], DisoNet [26], Where2comm [19], V2X-ViT [51], ERMVP [58], SICP [37], and mmCooper [30]) on both simulated (OPV2V) and real-world (DAIR-V2X) datasets, surpassing the second-best methods by 4.10%/3.25% and 5.18%/2.85% in AP@0.7/0.5, respectively. This superior performance stems from two key factors: first, the DCR module transmits compact codebook indices that are recon-

structured into point clouds via a shared codebook, preserving more raw spatial information than other baselines and thus enabling higher detection accuracy; second, the CAF module cascades the ego vehicle’s features using filtered collaborative information before pyramid-scale fusion, further strengthening perception of occluded or uncertain regions and boosting detection precision.

Communication Volume and Transmission Latency.

Fig. 6 shows that QPoint2Comm achieves the best performance with a low and stable communication volume of **14.95** (\log_2 scale), which is invariant to scene or traffic variations. This stability arises from the DCR module, which transmits compact discrete codebook indices instead of feature maps, resulting in a fixed and deterministic communication cost. As shown in Fig. 7, perception performance consistently degrades as communication latency increases; thus, lower bandwidth naturally implies lower latency. Our method not only incurs significantly lower bandwidth—leading to much lower latency in practice—but also outperforms other methods even under the same fixed-latency assumption, making the comparison conservative. For example, under a hypothetical communication setting with a bandwidth of 1 MB per 100 ms, our method requires only 0.032 MB ($2^{14.95}$ B) per frame, corresponding to 3.3 ms per frame, while Where2comm requires 6.15 MB ($2^{22.62}$ B), i.e., about 615 ms per frame. This highlights that our method would operate at much lower latency in practice.

Robustness to the Transmission Delay and Localization Error.

As shown in Fig. 7, our method consistently outperforms all baselines under both temporal and localization perturbations [30]. Across increasing delays (0, 100, 200, 300, 400,ms) and localization errors (0, 0.1, 0.2, 0.3, 0.4,m), performance degradation remains minimal. The robustness of QPoint2comm arises from three key components: (1) the DCR transmits compact codebook indices while preserving richer geometric information; (2) the Mask Training mechanism trains the network with randomly masked features, improving robustness and enhancing the model’s resistance to perturbations and noise; (3) the CAF cascades ego features before fusion using collaborative information, compensating for misalignment caused by both delays and localization errors. In contrast, When2com [31] and SICP [37] are less robust to real-world noise and can even underperform the non-fusion baseline, whereas QPoint2comm remains stable and reliable.

Ours vs Feature-level-quantization. Our method differs from feature-level quantization methods (e.g., CodeFilling [21]) in three aspects: we quantize raw LiDAR instead of latent features, reconstruct geometrically structured point clouds rather than feature maps, and transmit voxel-aligned indices with explicit spatial meaning instead of feature-semantic codes. As shown in Tab. 2, our method outperforms CodeFilling [21] on OPV2V under different latency

settings for both AP@0.5 and AP@0.7.

Table 2. Comparison with CodeFilling on OPV2V.

Method	0 ms	100 ms	200 ms	300 ms
	AP@0.5 / AP@0.7	AP@0.5 / AP@0.7	AP@0.5 / AP@0.7	AP@0.5 / AP@0.7
Ours	92.55 / 86.81	90.14 / 81.78	90.80 / 80.56	89.73 / 80.13
CodeFilling	90.82 / 88.19	85.29 / 59.63	75.16 / 58.67	73.69 / 57.13

Packet-Loss Tolerance. We evaluate QPoint2comm under random packet loss to simulate real-world vehicular communication (Tab. 3), where transmitted codebook indices are randomly dropped. To address this, Mask Training randomly masks features during training and learns a learnable feature, which is used at inference to fill missing regions caused by packet loss. Together with DCR, which preserves rich geometric information under limited bandwidth, QPoint2comm remains robust even under severe loss. Experiments on OPV2V and DAIR-V2X show that, despite gradual degradation, our method consistently outperforms most baselines, demonstrating reliable detection at high packet loss rates.

Table 3. Packet Loss Experiment: Detection Accuracy under Different Packet Loss Rates. Metric: AP@0.7 / AP@0.5 (\uparrow).

Packet Loss Rate	OPV2V	DAIR-V2X
	AP@0.7 / AP@0.5	AP@0.7 / AP@0.5
0	82.21 / 92.18	53.45 / 67.97
10%	77.78 / 89.06	52.09 / 64.32
20%	76.47 / 86.53	51.29 / 62.01
30%	75.84 / 85.44	50.84 / 60.64
40%	75.67 / 84.93	50.53 / 60.00

4.3. Ablation Study

Effect of Codebook Configuration. Effect of Codebook Configuration.

As shown in Tab. 4, detection performance peaks when the codebook size is 2048 with a vector dimensionality of 1024. In the DCR module, a smaller codebook limits the number of vectors available for quantization, reducing representation diversity and reconstruction fidelity, which can degrade downstream detection. Conversely, higher-dimensional vectors allow richer encoding of local geometric structures, enhancing feature quality and detection accuracy, but excessively large dimensions may introduce redundancy without significant gains. Therefore, a moderately large codebook with sufficient dimensionality provides an optimal trade-off, preserving detailed spatial information for accurate perception while maintaining low communication bandwidth.

Importance of Core Components.

We conduct an ablation study on OPV2V and DAIR-V2X in Tab. 5 evaluates the contribution of each module. Directly using raw point clouds—the only case without DCR—slightly increases accuracy but drastically raises communication cost, demonstrating that our DCR effectively balances accuracy detection with low bandwidth usage. Excluding the MSK mechanism leads to a clear drop in detection performance, even under ideal transmission conditions, indicating that random masking feature and learnable feature filling not only provide strong tolerance to packet loss but also enhance the model’s intrinsic robustness. Eliminating the CAF module removes the pre-fusion cascade of ego features, reducing

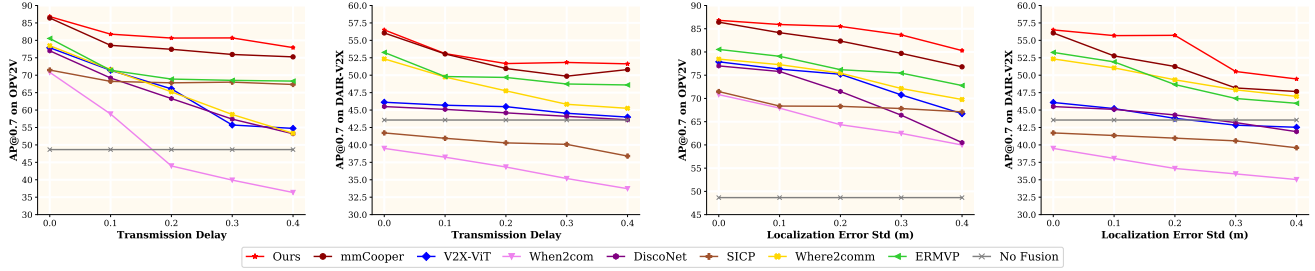


Figure 7. Robustness to the transmission delay and localization error on the OPV2V and DAIR-V2X.

Table 4. Effect of Codebook Configuration on Detection Performance. Metric: AP@0.7 / AP@0.5.

Dataset	Codebook Size	Code Dim	AP@0.7 / AP@0.5	Communication Volume
OPV2V	2048	1024	82.21 / 92.18	14.95
	1024	1024	81.43 / 91.64	14.81
	512	1024	81.33 / 91.33	14.66
	2048	512	81.92 / 92.09	14.95
DAIR-V2X	2048	1024	53.45 / 67.97	14.95
	1024	1024	53.21 / 66.67	14.81
	512	1024	53.18 / 64.60	14.66
	2048	512	52.44 / 62.18	14.95

the ego’s feature to perceive occluded and uncertain regions and thereby weakening both accuracy and robustness. The CFF and BFO modules further enhance performance. Although reconstructed collaborative features are informative, they may contain noise. CFF suppresses low-confidence regions to ensure reliable fusion, while BFO filters and refines bounding boxes to improve overall detection accuracy. Overall, these results show that DCR, MSK, and CAF are central to achieving efficient, robust, and high-performance collaborative perception, while all modules work synergistically to enhance overall system capability.

Comparison between Quantizing Point Cloud and Feature. As shown in Tab. 6, quantizing raw point clouds achieves higher detection accuracy than quantizing encoded features. Our approach compresses points into discrete codebook indices, which are transmitted and reconstructed at the ego agent, preserving rich spatial information essential for precise perception. In contrast, feature quantization compresses already encoded feature maps, which have already discarded some raw point cloud details during feature extraction. This secondary compression further reduces the fidelity of spatial and structural information, leading to lower detection performance. Therefore, point cloud quantization better balances low communication cost with high detection accuracy.

4.4. Qualitative Results

As shown in Fig. 8, our model detects more objects in DAIR-V2X scenes, while baseline methods often miss targets or produce misaligned bounding boxes. This advantage comes from multiple factors: DCR preserves richer raw spatial information, CAF strengthens ego features with filtered collaborative cues, and their integration improves robustness and localization accuracy under challenging con-

Table 5. Ablation Study of Individual Modules on Detection Performance (AP@0.7 / AP@0.5 \uparrow). Modules: Mask Training (MSK), Confidence-based Feature Filter (CFF), Cascade Attention Fusion (CAF), BBox Filter and Offset (BFO).

Dataset	MSK	CFF	CAF	BFO	AP@0.7 / AP@0.5
OPV2V	\times	\checkmark	\checkmark	\checkmark	80.52 / 91.79
	\checkmark	\times	\checkmark	\checkmark	81.19 / 91.49
	\checkmark	\checkmark	\times	\checkmark	79.29 / 90.51
	\checkmark	\checkmark	\checkmark	\times	79.15 / 91.61
	\checkmark	\checkmark	\checkmark	\checkmark	82.21 / 92.18
	Raw point cloud transmission				
DAIR-V2X	\times	\checkmark	\checkmark	\checkmark	52.60 / 67.80
	\checkmark	\times	\checkmark	\checkmark	50.19 / 66.22
	\checkmark	\checkmark	\times	\checkmark	49.13 / 64.91
	\checkmark	\checkmark	\checkmark	\times	51.70 / 66.76
	\checkmark	\checkmark	\checkmark	\checkmark	53.45 / 67.97
	Raw point cloud transmission				

Table 6. Comparison between Quantized Point Cloud and Quantized Intermediate Feature. Metric: AP@0.7 / AP@0.5.

Dataset	Quantized Point Cloud x_c	Quantized Feature F_c
	AP@0.7 / AP@0.5	AP@0.7 / AP@0.5
OPV2V	82.21 / 92.18	77.43 / 90.23
DAIR-V2X	53.45 / 67.97	49.06 / 66.03

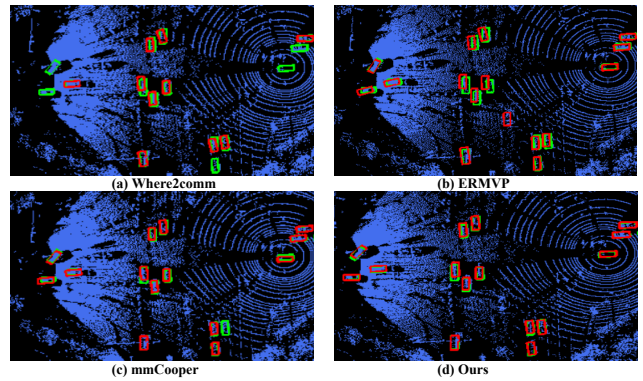


Figure 8. Visualization of detection results on the DAIR-V2X dataset. The green boxes correspond to ground truth annotations, while the red boxes show the predicted bounding boxes.

ditions.

5. Conclusion

In this paper, we present QPoint2comm, the first collaborative perception framework that employs the Discrete Point Cloud Representation module to quantize point clouds into compact discrete indices via shared codebooks for transmission, achieving low bandwidth while retaining rich raw information. Combined with the Mask Training, it is also the first framework to provide inherent tolerance to packet loss, ensuring stable perception even under high-loss scenarios. Furthermore, the Pyramid-scale with Cascade Attention Fusion cascades ego feature before fusion, improving robustness to occlusion and uncertainty. Experiments on OPV2V and DAIR-V2X show that QPoint2comm achieves superior accuracy with minimal bandwidth and remains robust under severe packet loss, validating its effectiveness and stability.

References

- [1] Ebtehal Turki Alotaibi, Shahad Saleh Alqefari, and Anis Koubaa. Lsar: Multi-uav collaboration for search and rescue missions. *IEEE Access*, 7:55817–55832, 2019. 1
- [2] Y. Bian, X. Wang, Y. Tan, M. Hu, C. Du, Z. Sun, and G. Guo. Distributed model predictive control of connected and automated vehicles with markov packet loss. *IEEE Transactions on Transportation Electrification*, 2024. 1
- [3] Lucas Caccia, Herke Van Hoof, Aaron Courville, and Joelle Pineau. Deep generative modeling of lidar data. In *2019 IEEE/RSJ International Conference on Intelligent Robots and Systems (IROS)*, pages 5034–5040. IEEE, 2019. 3
- [4] Nicolas Carion, Francisco Massa, Gabriel Synnaeve, Nicolas Usunier, Alexander Kirillov, and Sergey Zagoruyko. End-to-end object detection with transformers. In *European Conference on Computer Vision*, pages 213–229. Springer, 2020. 6
- [5] Hongyi Chen, Zhiping Lin, Yunjun Zhu, Jieliang Li, Liang Xiao, Yuliang Tang, and Yanyong Zhang. Reinforcement learning based collaborative perception for vehicular networks. In *2024 IEEE Global Communications Conference (GLOBECOM)*, pages 1997–2002. IEEE, 2024. 2, 3
- [6] Jinchao Chen, Qiuha Shu, Yantao Lu, Ying Zhang, and Yang Wang. Qctf: A quantized communication and transferable fusion framework for multi-agent collaborative perception. *IEEE Transactions on Intelligent Transportation Systems*, 2025. 2
- [7] Qi Chen, Sihai Tang, Qing Yang, and Song Fu. Cooper: Cooperative perception for connected autonomous vehicles based on 3d point clouds. In *2019 IEEE 39th International Conference on Distributed Computing Systems (ICDCS)*, pages 514–524. IEEE, 2019. 1, 2
- [8] Runjian Chen, Yao Mu, Runsen Xu, Wenqi Shao, Chenhan Jiang, Hang Xu, Yu Qiao, Zhenguo Li, and Ping Luo. Co3: Cooperative unsupervised 3d representation learning for autonomous driving. In *The Eleventh International Conference on Learning Representations*, 2023. 1
- [9] Siheng Chen, Baoan Liu, Chen Feng, Carlos Vallespi Gonzalez, and Carl K. Wellington. 3d point cloud processing and learning for autonomous driving: Impacting map creation, localization, and perception. *IEEE Signal Processing Magazine*, 38:68–86, 2021. 1
- [10] Ziming Chen, Yifeng Shi, and Jinrang Jia. Transiff: An instance-level feature fusion framework for vehicle-infrastructure cooperative 3d detection with transformers. In *Proceedings of the IEEE/CVF International Conference on Computer Vision*, pages 18205–18214, 2023. 1
- [11] Alexey Dosovitskiy, German Ros, Felipe Codevilla, Antonio Lopez, and Vladlen Koltun. CARLA: An open urban driving simulator. In *Proceedings of the 1st Annual Conference on Robot Learning*, pages 1–16. PMLR, 2017. 6
- [12] Mark Everingham, Luc Van Gool, Christopher K. I. Williams, John Winn, and Andrew Zisserman. The pascal visual object classes (voc) challenge. *International Journal of Computer Vision*, 88(2):303–338, 2010. 6
- [13] Zhengru Fang, Senkang Hu, Haonan An, Yuang Zhang, Jingjing Wang, Hangcheng Cao, Xianhao Chen, and Yuguang Fang. Pacp: Priority-aware collaborative perception for connected and autonomous vehicles. *IEEE Transactions on Mobile Computing*, 2024. 3
- [14] Zhengru Fang, Jingjing Wang, Yanan Ma, Yihang Tao, Yiqin Deng, Xianhao Chen, and Yuguang Fang. R-acp: Real-time adaptive collaborative perception leveraging robust task-oriented communications. *IEEE Journal on Selected Areas in Communications*, 2025. 2, 3
- [15] Jiahui Fu, Yue Gong, Luting Wang, Shifeng Zhang, Xu Zhou, and Si Liu. Generative map priors for collaborative bev semantic segmentation. In *Proceedings of the Computer Vision and Pattern Recognition Conference (CVPR)*, pages 11919–11928, 2025. 2
- [16] Rohit Girdhar, David F. Fouhey, Mikel Rodriguez, and Abhinav Gupta. Learning a predictable and generative vector representation for objects. In *European Conference on Computer Vision*, pages 484–499. Springer, 2016. 3
- [17] Ross Girshick. Fast r-cnn. In *Proceedings of the IEEE International Conference on Computer Vision*, pages 1440–1448, 2015. 5
- [18] Xunjie He, Yiming Li, Te Cui, Meiling Wang, Tong Liu, and Yufeng Yue. Robust collaborative perception against temporal information disturbance. In *2024 IEEE International Conference on Robotics and Automation (ICRA)*, pages 16207–16213. IEEE, 2024. 2, 3
- [19] Yue Hu, Shaoheng Fang, Zixing Lei, Yiqi Zhong, and Siheng Chen. Where2comm: Communication-efficient collaborative perception via spatial confidence maps. In *Advances in Neural Information Processing Systems*, pages 4874–4886, 2022. 1, 2, 5, 6, 4
- [20] Yue Hu, Shaoheng Fang, Weidi Xie, and Siheng Chen. Aerial monocular 3d object detection. *IEEE Robotics and Automation Letters*, 8:1959–1966, 2022. 1
- [21] Yue Hu, Juntong Peng, Sifei Liu, Junhao Ge, Si Liu, and Siheng Chen. Communication-efficient collaborative perception via information filling with codebook. In *2024 IEEE / CVF Computer Vision and Pattern Recognition Conference (CVPR)*, 2024. 2, 7
- [22] Tao Huang, Jianan Liu, Xi Zhou, Dinh C. Nguyen, Mostafa Rahimi Azghadi, Yuxuan Xia, Qing-Long Han, and Sumei Sun. V2x cooperative perception for autonomous driving: Recent advances and challenges. *arXiv preprint arXiv:2310.03525*, 2023. 2
- [23] Alex H. Lang, Sourabh Vora, Holger Caesar, Lubing Zhou, Jiong Yang, and Oscar Beijbom. Pointpillars: Fast encoders for object detection from point clouds. In *Proceedings of the IEEE/CVF Conference on Computer Vision and Pattern Recognition*, pages 12697–12705, 2019. 4, 6
- [24] Jesse Levinson, Jake Askeland, Jan Becker, Jennifer Dolson, David Held, Soeren Kammel, J Zico Kolter, Dirk Langer, Oliver Pink, Vaughan Pratt, et al. Towards fully autonomous driving: Systems and algorithms. In *2011 IEEE Intelligent Vehicles Symposium (IV)*, pages 163–168. IEEE, 2011. 1
- [25] Jinlong Li, Runsheng Xu, Xinyu Liu, Jin Ma, Zicheng Chi, Jiaqi Ma, and Hongkai Yu. Learning for vehicle-to-vehicle cooperative perception under lossy communication. *IEEE Transactions on Intelligent Vehicles*, 8(4):2650–2660, 2023. 3

- [26] Yiming Li, Shunli Ren, Pengxiang Wu, Siheng Chen, Chen Feng, and Wenjun Zhang. Learning distilled collaboration graph for multi-agent perception. In *Advances in Neural Information Processing Systems*, pages 29541–29552, 2021. 2, 6, 4
- [27] Zhiqi Li, Wenhai Wang, Hongyang Li, Enze Xie, Chonghao Sima, Tong Lu, Yu Qiao, and Jifeng Dai. Bevformer: Learning bird’s-eye-view representation from multi-camera images via spatiotemporal transformers. In *European Conference on Computer Vision*, pages 1–18. Springer, 2022. 1
- [28] Tsung-Yi Lin, Priya Goyal, Ross Girshick, Kaiming He, and Piotr Dollár. Focal loss for dense object detection. In *Proceedings of the IEEE International Conference on Computer Vision*, pages 2980–2988, 2017. 5
- [29] Zhiping Lin, Liang Xiao, Hongyi Chen, Zefang Lv, Yunjun Zhu, Yanyong Zhang, and Yong-Jin Liu. Edge-assisted collaborative collaborative perception against jamming and interference in vehicular networks. *IEEE Transactions on Wireless Communications*, 2024. 2, 3
- [30] Bingyi Liu, Jian Teng, Hongfei Xue, Enshu Wang, Chuanhui Zhu, Pu Wang, and Libing Wu. mmcooper: A multi-agent multi-stage communication-efficient and collaboration-robust cooperative perception framework. In *Proceedings of the IEEE/CVF International Conference on Computer Vision (ICCV)*, pages 28396–28406, 2025. 2, 5, 6, 7, 4
- [31] Yen-Cheng Liu, Junjiao Tian, Nathaniel Glaser, and Zsolt Kira. When2com: Multi-agent perception via communication graph grouping. In *Proceedings of the IEEE/CVF Conference on Computer Vision and Pattern Recognition*, pages 4106–4115, 2020. 2, 6, 7, 4
- [32] Yifan Lu, Quanhao Li, Baoan Liu, Mehrdad Dianati, Chen Feng, Siheng Chen, and Yanfeng Wang. Robust collaborative 3d object detection in presence of pose errors. In *2023 IEEE International Conference on Robotics and Automation (ICRA)*, pages 4812–4818. IEEE, 2023. 1
- [33] Chris J. Maddison, Andriy Mnih, and Yee Whye Teh. The concrete distribution: A continuous relaxation of discrete random variables. *arXiv preprint arXiv:1611.00712*, 2016. 5
- [34] Zonglin Meng, Xin Xia, Runsheng Xu, Wei Liu, and Jiaqi Ma. Hydro-3d: Hybrid object detection and tracking for cooperative perception using 3d lidar. *IEEE Transactions on Intelligent Vehicles*, 2023. 1
- [35] Moritz Menze and Andreas Geiger. Object scene flow for autonomous vehicles. In *Proceedings of the IEEE Conference on Computer Vision and Pattern Recognition*, pages 3061–3070, 2015. 6
- [36] Kazuto Nakashima and Ryo Kurazume. Lidar data synthesis with denoising diffusion probabilistic models. In *Proceedings of the International Conference on Robotics and Automation (ICRA)*, pages 14724–14731, 2024. 3
- [37] D. Qu, Q. Chen, T. Bai, et al. Sicp: Simultaneous individual and cooperative perception for 3d object detection in connected and automated vehicles. In *2024 IEEE/RSJ International Conference on Intelligent Robots and Systems (IROS)*, pages 8905–8912. IEEE, 2024. 6, 7, 4
- [38] Haoxi Ran, Vitor Guizilini, and Yue Wang. Towards realistic scene generation with lidar diffusion models. In *Proceedings of the IEEE/CVF Conference on Computer Vision and Pattern Recognition*, pages 14738–14748, 2024. 3
- [39] Joseph Redmon, Santosh Divvala, Ross Girshick, and Ali Farhadi. You only look once: Unified, real-time object detection. In *Proceedings of the IEEE Conference on Computer Vision and Pattern Recognition (CVPR)*, pages 779–788, 2016. 1
- [40] Axel Sauer, Kashyap Chitta, Jens Müller, and Andreas Geiger. Projected gans converge faster. In *Advances in Neural Information Processing Systems*, pages 17480–17492, 2021. 3
- [41] Jingyue Shi, Junhui Zhao, Li Zhuo, Xiaoming Wang, Xiaohuang Zhan, and Haitao Liu. V2v cooperative perception with adaptive communication loss for autonomous driving. *IEEE Transactions on Intelligent Transportation Systems*, 2025. 2, 3
- [42] Shuyao Shi, Jiahe Cui, Zehao Jiang, Zhenyu Yan, Guoliang Xing, Jianwei Niu, and Zhenchao Ouyang. Vips: Real-time perception fusion for infrastructure-assisted autonomous driving. In *Proceedings of the 28th Annual International Conference on Mobile Computing and Networking*, pages 133–146, 2022. 2
- [43] A. Singh, T. Jain, and S. Sukhbaatar. Learning when to communicate at scale in multiagent cooperative and competitive tasks. *arXiv preprint arXiv:1812.09755*, 2018. 2
- [44] Zhiying Song, Fuxi Wen, Hailiang Zhang, and Jun Li. A cooperative perception system robust to localization errors. In *2023 IEEE Intelligent Vehicles Symposium (IV)*, pages 1–6. IEEE, 2023. 2
- [45] Hao Su, Shin’Ichi Arakawa, and Masayuki Murata. 3d multi-object tracking based on two-stage data association for collaborative perception scenarios. In *2023 IEEE Intelligent Vehicles Symposium (IV)*, pages 1–7. IEEE, 2023. 2
- [46] Tao Tang, Chaokun Zhang, Gong Chen, and Jinlong E. Rocooper: Robust cooperative perception under vehicle-to-vehicle communication impairments. In *IEEE INFOCOM 2025 - IEEE Conference on Computer Communications*, pages 1–10. IEEE, 2025. 2, 3
- [47] Aaron van den Oord, Oriol Vinyals, and Koray Kavukcuoglu. Neural discrete representation learning. In *Advances in Neural Information Processing Systems*, 2017. 2, 3, 4
- [48] Tsun-Hsuan Wang, Sivabalan Manivasagam, Ming Liang, Bin Yang, Wenyuan Zeng, and Raquel Urtasun. V2vnet: Vehicle-to-vehicle communication for joint perception and prediction. In *European Conference on Computer Vision*, pages 605–621. Springer, 2020. 1
- [49] Yuwen Xiong, Wei-Chiu Ma, Jingkang Wang, and Raquel Urtasun. Learning compact representations for lidar completion and generation. In *CVPR*, pages 1074–1083, 2023. 3
- [50] Runsheng Xu, Yi Guo, Xu Han, Xin Xia, Hao Xiang, and Jiaqi Ma. Opencda: An open cooperative driving automation framework integrated with co-simulation. In *2021 IEEE International Intelligent Transportation Systems Conference (ITSC)*, pages 1155–1162. IEEE, 2021. 6

- [51] Runsheng Xu, Hao Xiang, Zhengzhong Tu, Xin Xia, Ming-Hsuan Yang, and Jiaqi Ma. V2x-vit: Vehicle-to-everything cooperative perception with vision transformer. In *European Conference on Computer Vision*, pages 107–124. Springer, 2022. 2, 6, 4
- [52] Runsheng Xu, Hao Xiang, Xin Xia, Xu Han, Jinlong Li, and Jiaqi Ma. Opv2v: An open benchmark dataset and fusion pipeline for perception with vehicle-to-vehicle communication. In *2022 International Conference on Robotics and Automation (ICRA)*, pages 2583–2589. IEEE, 2022. 2, 6, 4
- [53] Runsheng Xu, Weizhe Chen, Hao Xiang, Xin Xia, Lantao Liu, and Jiaqi Ma. Model-agnostic multi-agent perception framework. In *2023 IEEE International Conference on Robotics and Automation (ICRA)*, pages 1471–1478. IEEE, 2023. 2
- [54] Chenyu Yang, Yuntao Chen, Hao Tian, Chenxin Tao, Xizhou Zhu, Zhaoxiang Zhang, Gao Huang, Hongyang Li, Yu Qiao, Lewei Lu, et al. Bevformer v2: Adapting modern image backbones to bird’s-eye-view recognition via perspective supervision. In *Proceedings of the IEEE/CVF Conference on Computer Vision and Pattern Recognition*, pages 17830–17839, 2023. 1
- [55] Yujia Yang, Quan Yuan, Yang Li, Guiyang Luo, Xiaoyuan Fu, Jiajia Liu, and Jinglin Li. Utility - aware resource allocation for multi - group collaborative perception system. *IEEE Internet of Things Journal*, 2025. 2, 3
- [56] Haibao Yu, Yizhen Luo, Mao Shu, Yiyi Huo, Zebang Yang, Yifeng Shi, Zhenglong Guo, Hanyu Li, Xing Hu, Jirui Yuan, et al. Dair-v2x: A large-scale dataset for vehicle-infrastructure cooperative 3d object detection. In *Proceedings of the IEEE/CVF Conference on Computer Vision and Pattern Recognition*, pages 21361–21370, 2022. 2, 6, 4
- [57] Xumin Yu, Lulu Tang, Yongming Rao, Tiejun Huang, Jie Zhou, and Jiwen Lu. Point-bert: Pre-training 3d point cloud transformers with masked point modeling. In *Proceedings of the IEEE Conference on Computer Vision and Pattern Recognition (CVPR)*, pages 19313–19322, 2022. 3
- [58] Jingyu Zhang, Kun Yang, Yilei Wang, Hanqi Wang, Peng Sun, and Liang Song. Ermvp: Communication-efficient and collaboration-robust multi-vehicle perception in challenging environments. In *Proceedings of the IEEE/CVF Conference on Computer Vision and Pattern Recognition*, pages 12575–12584, 2024. 2, 6, 4
- [59] Qingzhao Zhang, Xumiao Zhang, Ruiyang Zhu, Fan Bai, Mohammad Naserian, and Z Morley Mao. Robust real-time multi-vehicle collaboration on asynchronous sensors. In *Proceedings of the 29th Annual International Conference on Mobile Computing and Networking*, pages 1–15, 2023. 2
- [60] Xumiao Zhang, Anlan Zhang, Jiachen Sun, Xiao Zhu, Y Ethan Guo, Feng Qian, and Z Morley Mao. Emp: Edge assisted multi-vehicle perception. In *Proceedings of the 27th Annual International Conference on Mobile Computing and Networking*, pages 545–558, 2021. 1, 2
- [61] Yuang Zhang, Haonan An, Zhengru Fang, Guowen Xu, Yuan Zhou, Xianhao Chen, and Yuguang Fang. Smartcooper: Vehicular collaborative perception with adaptive fusion and judger mechanism. In *2024 IEEE International Conference on Robotics and Automation (ICRA)*, pages 4450–4456. IEEE, 2024. 3
- [62] Zixu Zhang and Jaime F. Fisac. Safe occlusion-aware autonomous driving via game-theoretic active perception. *arXiv preprint arXiv:2105.08169*, 2021. 1
- [63] Vlas Zyrianov, Xiyue Zhu, and Shenlong Wang. Learning to generate realistic lidar point clouds. In *Proceedings of the European Conference on Computer Vision (ECCV)*, pages 17–35, 2022. 3

Send Less, Perceive More: Masked Quantized Point Cloud Communication for Loss-Tolerant Collaborative Perception

Supplementary Material

6. Overview

The supplementary material is organized into the following sections:

1. Sec. 7: The Overall System Pipeline
 - (a) Sec. 7.1: The Training Pipeline of Discrete Point Cloud Representation
 - (b) Sec. 7.2: The Training Pipeline of the Mask Fusion and Detection
 - (c) Sec. 7.3: The Inference Pipeline of Our Proposed QPoint2comm
2. Sec. 8: The Additional Experimental Results on OPV2V and DAIR-V2X Datasets
 - (a) Sec. 8.1: Implementation Details
 - (b) Sec. 8.2: Supplements on Localization Errors, Transmission Delays and Heading Errors
 - (c) Sec. 8.3: Ablation Study on Separated Backbone and Shared Backbone
3. Sec. 9: The Additional Qualitative Results on Point Cloud Reconstruction and Detection Results
 - (a) Sec. 9.1: Visualization of Point Cloud Reconstruction
 - (b) Sec. 9.2: Visualization of Detection Results
4. Sec. 10: Quantitative comparison of original and reconstructed point cloud
5. Sec. 11: Feature-level quantization vs Ours
6. Sec. 12: More quantitative results under different settings

7. The System Pipeline of our models

Our model is trained in two stages: the first stage learns the discrete representation of point cloud (Sec. 7.1), and the second stage focuses on mask training, feature fusion, and bounding-box generation (Sec. 7.2). After these two stages, we further describe the inference pipeline of the QPoint2comm system (Sec. 7.3).

7.1. The Training Pipeline of Discrete Point Cloud Representation Module

The training pipeline of the **Discrete Point Cloud Representation (DCR)** module is illustrated in Algorithm 1. The algorithm learns discrete representations of LiDAR point cloud by jointly training the occupancy and intensity branches, enabling the model to capture complementary geometric and reflectance characteristics and providing structured encodings for downstream collaborative perception tasks.

Grid-based Preprocessing: Grid-based preprocessing

converts the raw LiDAR point cloud x into two independent tensors: an occupancy tensor $X_{\text{occ}} \in \{0, 1\}^{H \times W \times L}$, indicating whether each grid contains points, and an intensity tensor $X_{\text{int}} \in [0, 1]^{H \times W \times L}$, representing normalized reflectivity. This discretization captures the spatial structure of the point cloud.

Codebook Training: Branch-specific training is performed, with occupancy and intensity learned independently. In the occupancy branch, the encoder E_{occ} maps X_{occ} to latent features Z_{occ} , which are then quantized using a learnable codebook \mathcal{E}_{occ} to produce discrete embeddings \hat{Z}_{occ} . A decoder Dec_{occ} , combined with grid-wise Gaussian parameters, reconstructs the occupancy tensor. The training objective includes a vector quantization loss $\mathcal{L}_{\text{vq,occ}}$ and a reconstruction loss \mathcal{L}_{occ} based on binary cross-entropy. The intensity branch uses a similar encoder-codebook-decoder pipeline ($E_{\text{int}}, \mathcal{E}_{\text{int}}, \text{Dec}_{\text{int}}$) with supervision via mean squared error (\mathcal{L}_{int}) and quantization loss ($\mathcal{L}_{\text{vq,int}}$). Unlike occupancy, the intensity decoder does not apply Gaussian sampling, producing the same reflection value for all points within a given occupied grid. The codebooks for the occupancy and intensity branches are updated via K-means clustering to adaptively capture their respective distributions. The framework maintains separate encoders, decoders, and codebooks for occupancy and intensity, producing structured, type-specific discrete representations. This design enables efficient discrete representations for cross-agent transmission and collaborative perception.

7.2. The Training Pipeline of the Mask Fusion and Detection Module

As shown in Algorithm 2, the **Mask Fusion and Detection** module is trained using the raw ego point cloud x_e , collaborative point clouds $\{x_c\}^{N_c}$, and ground-truth bounding boxes B_{gt} , and produces the trained detection parameters Θ_{det} .

Mask Training: Ego features F_e are first extracted from x_e . Each collaborative point cloud x_c is processed to obtain features \hat{F} , where random regions are masked and replaced with learnable features $f_{\text{learnable}}$ to produce the filled collaborative features F_c .

Feature Fusion and Detection: The collaborative features F_c are first filtered using a Confidence-based Feature Filter module (CFF) to produce \hat{F}_c and \hat{B}_c . Then, cascade ego feature F_e with filtered collaborative features \hat{F}_c to obtain cascaded ego feature \hat{F}_e . Pyramid-scale fusion aggregates information across different feature scales to ob-

Algorithm 1: The Training Pipeline of the Discrete Point Cloud Representation

Input: Raw LiDAR point cloud from collaborative agents $\{x_c\}^{N_c}$.

Output: Trained occupancy encoder E_{occ} , decoder Dec_{occ} , codebook $\mathcal{E}_{\text{occ}} = \{e_k^{\text{occ}}\}_{k=1}^{K_{\text{occ}}}$,
Intensity encoder E_{int} , decoder Dec_{int} , codebook $\mathcal{E}_{\text{int}} = \{e_k^{\text{int}}\}_{k=1}^{K_{\text{int}}}$.

1. Voxelization: Discretize x_c into two independent tensors:

- Occupancy tensor $X_{\text{occ}} \in \{0, 1\}^{\mathcal{H} \times \mathcal{W} \times \mathcal{L}}$;
- Intensity tensor $X_{\text{int}} \in [0, 1]^{\mathcal{H} \times \mathcal{W} \times \mathcal{L}}$.

2. Separate Training for Each Branch: for $branch \in \{\text{occupancy}, \text{intensity}\}$ do

 if $branch$ is occupancy then

2.1 Encoding: Obtain latent features $Z_{\text{occ}} = E_{\text{occ}}(X_{\text{occ}}) \in \mathbb{R}^{h \times w \times D_{\text{occ}}}$.

2.2 Vector Quantization: For each $z_i^{\text{occ}} \in Z_{\text{occ}}$, find nearest codebook entry:

$$k_{\text{occ}}^* = \arg \min_k \|z_i^{\text{occ}} - e_k^{\text{occ}}\|_2^2, \quad \hat{Z}_{\text{occ}} = q_{\text{occ}}(Z_{\text{occ}}) = \{e_{k_{\text{occ}}^*}^{\text{occ}}\}.$$

2.3 Reconstruction: Reconstruct occupancy tensor:

$$\hat{X}_{\text{occ}} = \text{Dec}_{\text{occ}}(\hat{Z}_{\text{occ}}; \mathcal{N}(\mu_{\text{occ}}, \Sigma_{\text{occ}})).$$

2.4 Loss Computation:

$$\mathcal{L}_{\text{occ}} = \mathcal{L}_{\text{vq,occ}} + \lambda_{\text{occ}} \mathcal{L}_{\text{occ.reconstruct}}.$$

2.5 Codebook Update: Update \mathcal{E}_{occ} via exponential moving average.

 else

2.6 Encoding: Obtain latent features $Z_{\text{int}} = E_{\text{int}}(X_{\text{int}}) \in \mathbb{R}^{h \times w \times D_{\text{int}}}$.

2.7 Vector Quantization: For each $z_i^{\text{int}} \in Z_{\text{int}}$, find nearest codebook entry:

$$k_{\text{int}}^* = \arg \min_k \|z_i^{\text{int}} - e_k^{\text{int}}\|_2^2, \quad \hat{Z}_{\text{int}} = q_{\text{int}}(Z_{\text{int}}) = \{e_{k_{\text{int}}^*}^{\text{int}}\}.$$

2.8 Reconstruction: Reconstruct intensity tensor:

$$\hat{X}_{\text{int}} = \text{Dec}_{\text{int}}(\hat{Z}_{\text{int}}).$$

2.9 Loss Computation:

$$\mathcal{L}_{\text{int}} = \mathcal{L}_{\text{vq,int}} + \lambda_{\text{int}} \mathcal{L}_{\text{int.reconstruct}}.$$

2.10 Codebook Update: Update \mathcal{E}_{int} via exponential moving average.

3. Output: Store all trained components $\{E_{\text{occ}}, \text{Dec}_{\text{occ}}, \mathcal{E}_{\text{occ}}\}$ and $\{E_{\text{int}}, \text{Dec}_{\text{int}}, \mathcal{E}_{\text{int}}\}$ as Θ_{DCR} .

tain fused features \mathcal{F}_i , which are then fed into the detection head to predict fused bounding boxes B_{fused} . Collaborative bounding boxes \hat{B}_c is corrected using the BBox Filter and Offset (BFO) module to produce B_{offset} . The final bounding boxes B_{final} are obtained by merging B_{fused} and B_{offset} .

Loss Computation: The predicted bounding boxes B_{final} are compared against the ground-truth B_{gt} to compute the total loss L_{total} , which includes regression, classification, offset, and confidence score terms. This loss is used to optimize the detection model parameters Θ_{det} .

7.3. The Inference Pipeline of the Qpoint2comm

As illustrated in Algorithm 3, the inference pipeline of QPoint2comm takes as input the raw ego LiDAR point

cloud x_e , raw collaborative point clouds $\{x_c\}^{N_c}$, and the trained parameters of the discrete point cloud representation (DCR) Θ_{DCR} and detection module Θ_{det} . The output is the final bounding boxes B_{final} .

Discrete Point Cloud Representation: Each collaborative point cloud x_c is first encoded into discrete codebook indices using the DCR module. These indices are transmitted under lossy network conditions and subsequently decoded to reconstruct the point cloud \hat{x}_c in the ego vehicle’s coordinate frame. This process compresses the collaborative data for efficient transmission while preserving the essential spatial and intensity information necessary for downstream perception tasks.

Fusion and Detection: First, ego features F_e are ex-

Algorithm 2: The Training Pipeline of the Mask Fusion and Detection

Input: Raw ego LiDAR point cloud x_e , raw collaborative point clouds $\{x_c\}^{N_c}$, and ground-truth bounding boxes B_{gt} .

Output: Trained detection model parameters Θ_{det} .

1. Mask Training:**1.1 Ego Feature Extraction:**

$$F_e = \psi_E(x_e).$$

1.2 Collaborative Feature Masking and Filling:

for each collaborative point cloud x_c do

 Extract features masking:

$$\tilde{F} = \mathcal{M}_r(\psi_C(x_c)).$$

 Apply learnable feature filling:

 Masked features in \tilde{F} are replaced with the learnable feature $f_{learnable}$, producing F_c .

2. Feature Fusion and Detection:**2.1 Confidence-based Feature Filter:**

for each filled collaborative feature F_c do

$$B_c = \text{Detector}(F_c), \quad \hat{G}_{f,b} = G_{f,b} \odot \mathbb{I}_{\{G_{f,b} > \tau_p\}} \odot \mathcal{G}_\sigma(G_{f,b}), \quad \hat{F}_c = \hat{G}_f \otimes F_c, \quad \hat{B}_c = \hat{G}_b \otimes B_c.$$

2.2 Ego Feature Cascade:

Cascade ego feature with collaborative features:

$$A_{add} = H_{add}(\text{Attn}(F_e, \hat{F}_c, \hat{F}_c)) + F_e, \quad A_{mul} = H_{mul}(\text{Attn}(F_e, \hat{F}_c, \hat{F}_c)) \otimes F_e, \quad \hat{F}_e = \sigma(W_g) \otimes A_{add} + (1 - \sigma(W_g)) \otimes A_{mul}.$$

2.3 Pyramid-scale Feature Fusion:

for each filtered collaborative feature \hat{F}_c do

$$\mathcal{F}_i^l = \text{NeighborCrossAttn}(MLP(\hat{F}_e^l), \hat{F}_c^l, \hat{F}_c^l), \quad l = 1, 2, 3, \quad \mathcal{F}_i = \text{Concat}(\mathcal{F}_i^1, \mathcal{F}_i^2, \mathcal{F}_i^3).$$

2.4 Detection Head:

Predict bounding boxes:

$$B_{fused} = \text{Detector}(\mathcal{F}_i).$$

2.5 BBox Filter and Offset:

$$(\text{off}, \text{score}) = \text{Deformable-Bbx-Attention}(\mathcal{F}_i, \hat{B}_c), \quad B_{offset} = \phi(\hat{B}_c, \text{off}, \text{score}).$$

2.6 Final Fusion:

$$B_{final} = \text{Merge}(B_{fused}, B_{offset}).$$

3. Loss Computation:

Compute the training loss between the final predictions B_{final} and ground-truth B_{gt} :

$$L_{total} = L_{reg} + L_{cls} + L_{off} + L_{score}.$$

Output: Return trained detection model parameters Θ_{det} .

tracted from the ego point cloud x_e . Each reconstructed collaborative point cloud \hat{x}_c is processed to extract features \tilde{F} , where missing regions are filled using learnable feature $f_{learnable}$ to produce F_c . The collaborative features F_c and corresponding bounding boxes B_c are filtered with the CFF module to obtain filtered features \hat{F}_c and bounding boxes \hat{B}_c . Then, cascade ego feature F_e with filtered collaborative

features \hat{F}_c to obtain cascaded ego feature \hat{F}_e . Pyramid-scale fusion combines \hat{F}_e with \hat{F}_c across different scales to obtain fused features \mathcal{F}_i . The fused features are fed into the detection head to predict bounding boxes B_{fused} . In parallel, collaborative bounding boxes \hat{B}_c are refined using the BFO module to produce B_{offset} . Finally, the fused and refined bounding boxes are merged to produce the final predictions

B_{final} .

This pipeline effectively integrates the ego vehicle’s information with reconstructed collaborative point clouds, compensates for missing or occluded regions in the collaborative data, and produces robust and accurate 3D object detections, ensuring reliable perception even under lossy communication conditions.

8. Additional Experimental Results on OPV2V and DAIR-V2X

8.1. Implementation Details

DCR Module. On the OPV2V [52] and DAIR-V2X [56] datasets, the grid size is set to $0.15625 \times 0.15625 \times 0.15$ meters along the x , y , and z . The latent representation has a spatial resolution of $h \times w = 80 \times 1440$ and a channel dimension of $D = 1024$, resulting in $h \times w = 11520$ vectors of dimension D to be quantized. The vector quantizer maintains reliable codebook usage through a reservoir-based refresh and periodic K-means reinitialization when code frequency falls below the dead limit (256), ensuring stable and effective quantization throughout training.

Detection Module. On the OPV2V [52] and DAIR-V2X [56] datasets, the voxel grid size encoded by the backbone encoder is set to $0.4 \times 0.4 \times 4$ meters along the x , y , and z . The resulting bird’s-eye-view (BEV) feature maps, shared among collaborative agents, have channel dimension $C = 64$ and spatial dimensions $H \times W = 100 \times 352$ for OPV2V, and $H \times W = 100 \times 252$ for DAIR-V2X. Shared bounding boxes among agents are parameterized by their center coordinates, object dimensions (length, width, height), and heading angle. The detection head is implemented using two separate 1×1 convolutional layers, one for regression of geometric parameters and the other for classification of object confidence scores.

8.2. Supplements on Localization Errors, Transmission Delays and Heading Errors

We evaluate the robustness of the proposed method on the OPV2V and DAIR-V2X datasets under three types of perturbations: localization errors, transmission delays, and heading noise. Localization errors are sampled from a Gaussian distribution with zero mean and standard deviation $\sigma \in \{0.0, 0.1, 0.2, 0.3, 0.4\}$ m, and the results in Fig. 9 indicate that the method consistently outperforms existing state-of-the-art approaches [19, 26, 30, 31, 37, 51, 52, 58], across all levels of error. Similarly, when evaluating the impact of transmission delays of $\{0, 100, 200, 300, 400\}$ ms, Fig. 10 shows that the proposed approach maintains superior performance compared to baseline methods under all delay conditions. Finally, as shown in Fig. 11, the method demonstrates robustness to heading errors ranging from $\{0.0, 0.1, 0.2, 0.3, 0.4\}^\circ$, consistently outperforming other

models despite the gradual decrease in detection accuracy with increasing noise. Collectively, these results highlight the robustness of the proposed method to common real-world perturbations in collaborative perception scenarios.

8.3. Ablation Study on Separated Backbone and Shared Backbone

We conducted experiments on OPV2V and DAIR-V2X using a PointPillars-based [23] backbone, comparing separate encoders with a shared encoder, as shown in Tab. 7. In the separated-backbone setting, the ego LiDAR point cloud and the reconstructed collaborative point clouds are processed by two independent backbone encoders, allowing each encoder to better model the distinct feature characteristics of ego point cloud and collaborative point clouds. By contrast, a shared encoder must handle both inputs with the same set of parameters, making it difficult to capture their different feature distributions. As evidenced by the experimental results, the separated-backbone configuration consistently achieves higher detection accuracy, demonstrating its superiority over the shared-backbone alternative.

Table 7. Comparison between Separated Backbone and Shared Backbone. Metric: AP@0.7 / AP@0.5.

Dataset	Separated Backbone	Shared Backbone
	AP@0.7 / AP@0.5	AP@0.7 / AP@0.5
OPV2V	82.21 / 92.18	79.87 / 91.60
DAIR-V2X	53.45 / 67.97	50.36 / 65.55

9. Additional Qualitative Results

9.1. Visualization of Original and Reconstructed Point Clouds

We visualize the effectiveness of the Discrete Point Cloud Representation (DCR) module by comparing top-down views of the original point clouds with those reconstructed from transmitted discrete indices. As shown in Fig. 12 and Fig. 13 for the OPV2V and DAIR-V2X datasets, respectively, the reconstructed point clouds retain the spatial structure and geometric layout of the original scenes while preserving essential object information. These results highlight that DCR enables compact transmission without significant loss of critical spatial details, supporting accurate and robust collaborative perception.

9.2. Visualization of Detection Results

We further present additional qualitative results on the DAIR-V2X dataset. As shown in Fig. 14, the visualizations across diverse road scenarios indicate that our proposed method achieves highly accurate object detection, successfully capturing the majority of ground-truth instances with negligible false positives. This strong performance stems

Algorithm 3: Inference Pipeline of QPoint2comm

Input: Raw ego LiDAR point cloud x_e , raw collaborative point clouds $\{x_c\}^{N_c}$, trained DCR parameters Θ_{DCR} , trained detection parameters Θ_{det} .

Output: Final fused bounding boxes B_{final} .

1. Discrete Point Cloud Representation:

for each collaborative point cloud x_c **do**

 └ Encode x_c into discrete indices, transmit in lossy condition, and decode to obtain reconstructed point cloud \hat{x}_c .

2. Fusion and Detection:

2.1 Ego Feature Extraction: $F_e = \psi_E(x_e)$.

2.2 Learnable Feature Filling:

Extract features: $\tilde{F} = \psi_C(\hat{x}_c)$.

Let \mathcal{S} denote the set of feature locations that are missing due to packet loss.

for each feature location j **do**

if $j \in \mathcal{S}$ **then**

 └ Fill the missing region with the learnable representation: $F_c[j] = f_{learnable}$.

else

 └ Use the reconstructed collaborative feature: $F_c[j] = \tilde{F}[j]$.

2.3 Confidence-based Feature Filter: Filter unreliable regions in collaborative features F_c to get \hat{F}_c and filter collaborative bounding boxes B_c to get \hat{B}_c .

2.4 Ego Feature cascade : Cascade ego feature F_e with \hat{F}_c to obtain cascaded ego feature \hat{F}_e .

2.5 Pyramid-scale Collaborative Fusion: Fuse cascaded ego feature \hat{F}_e with \hat{F}_c across multiple-scale to get fused features \mathcal{F}_i .

2.6 Detection Head: Fused bounding boxes, $B_{fused} = \text{Detector}(\mathcal{F}_i)$.

2.7 BBox Filter and Offset: Refine collaborative bounding boxes \hat{B}_c using BFO module to obtain B_{offset} .

2.8 Final Merge: Merge fused and refined boxes to produce final predictions: $B_{final} = \text{Merge}(B_{fused}, B_{offset})$.

Output: Return final bounding boxes B_{final} .

from two key designs: Discrete Point Cloud Representation (DCR) preserves rich raw geometric information, enabling more faithful reconstruction and clearer object shapes after transmission, while Cascade Attention Fusion (CAF) cascades ego features before fusion, effectively compensating for occluded regions. Together, these components yield highly consistent and robust perception under complex and dynamic driving environments.

10. Quantitative comparison of original and reconstructed point cloud

We report the quantitative Chamfer Distance between the original and reconstructed point clouds in Tab. 8, indicating that the reconstruction preserves the original point cloud geometry well.

Table 8. Chamfer Distance on OPV2V and DAIR-V2X dataset.

Dataset	OPV2V	DAIR-V2X
Chamfer Distance (m)	0.0572	0.0516

11. Feature-level quantization vs Ours

Our method differs fundamentally from feature-level quantization methods (e.g., CodeFilling) in three key aspects, namely the quantization target, the reconstruction objective, and the semantic meaning of transmitted indices:

- **Quantization target.** We quantize LiDAR, whereas feature-level methods quantize latent semantic features.
- **Reconstruction objective.** We reconstruct LiDAR with explicit spatial structure, while feature-level methods reconstruct feature maps without geometric form.
- **Semantic meaning of transmitted indices.** Our discrete indices are voxel-aligned and spatially grounded, carrying explicit geometric meaning, whereas feature-level methods transmit feature-semantic indices without direct geometric correspondence.

12. More quantitative results under different settings

We report AP@0.7 results under varying communication latency, localization error, and heading error in Tabs. 9 to 11, demonstrating that our method consistently achieves superior performance over prior approaches under all settings.

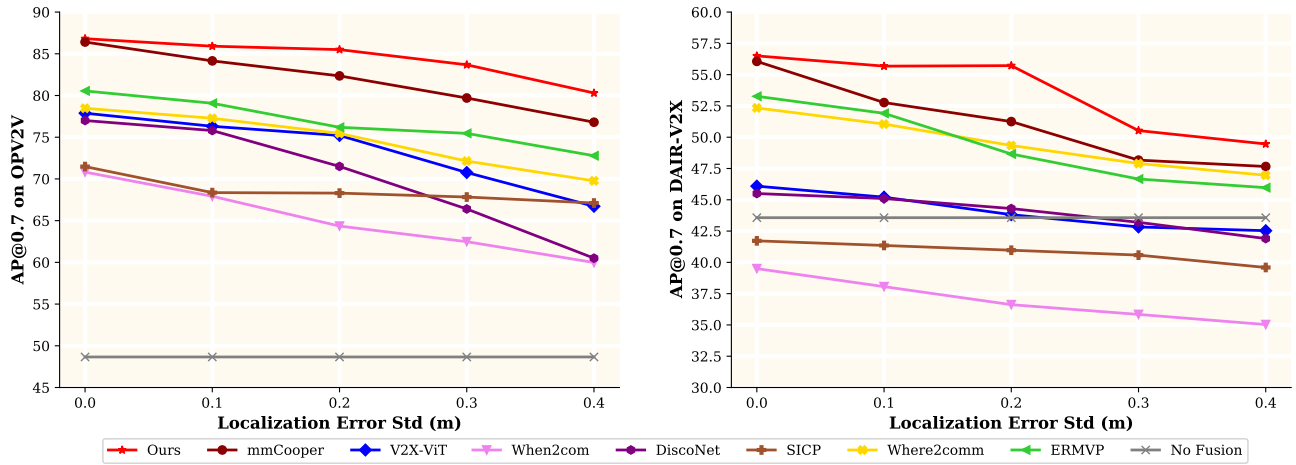


Figure 9. Robustness to the localization error on the OPV2V and DAIR-V2X datasets.

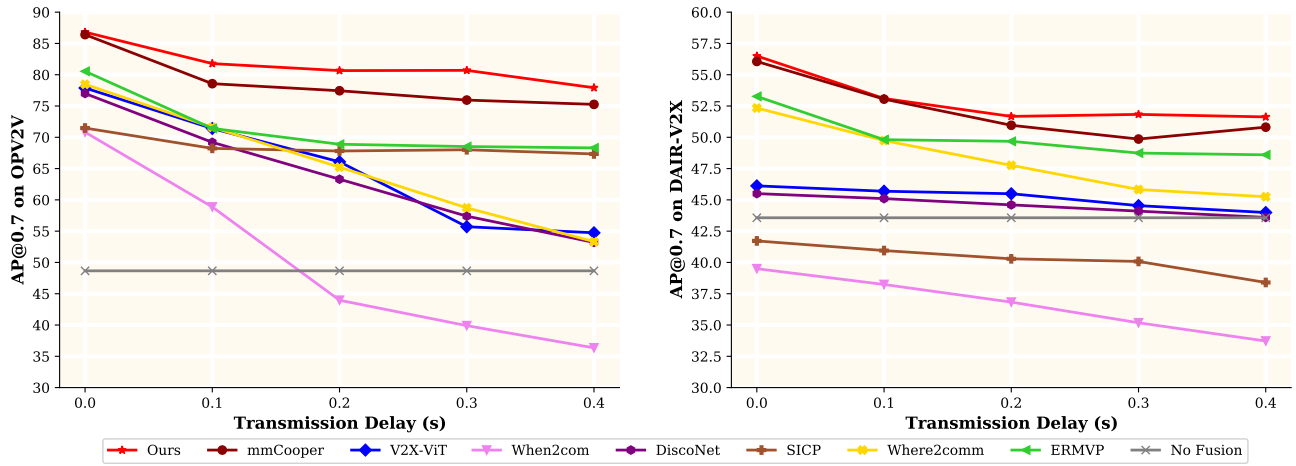


Figure 10. Robustness to the transmission delay on the OPV2V and DAIR-V2X datasets.

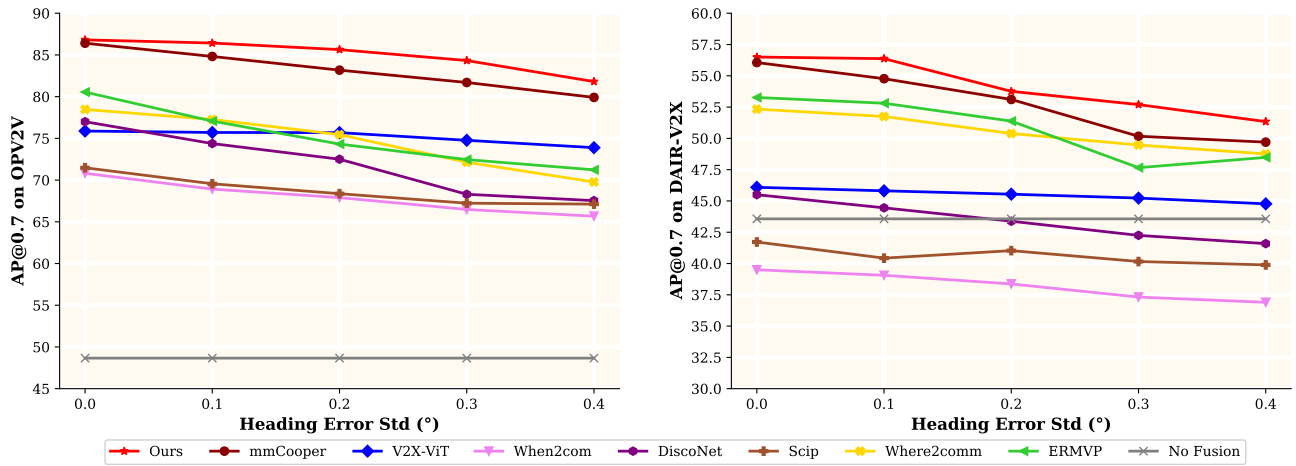


Figure 11. Robustness to the heading error on the OPV2V and DAIR-V2X datasets.

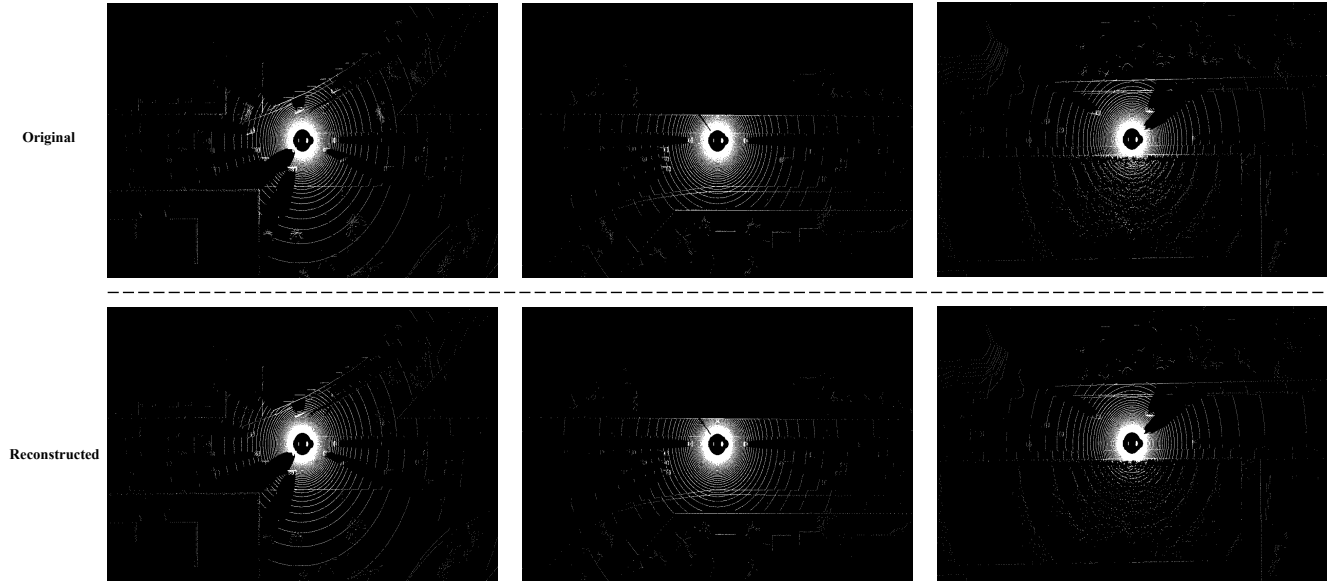


Figure 12. Visualization of BEV representations on the OPV2V dataset. The top row shows the original LiDAR point cloud BEV maps, while the bottom row presents the reconstructed BEV maps obtained from the transmitted discrete indices. The high structural consistency indicates that the DCR module effectively preserves the geometric and semantic information of the original scenes.

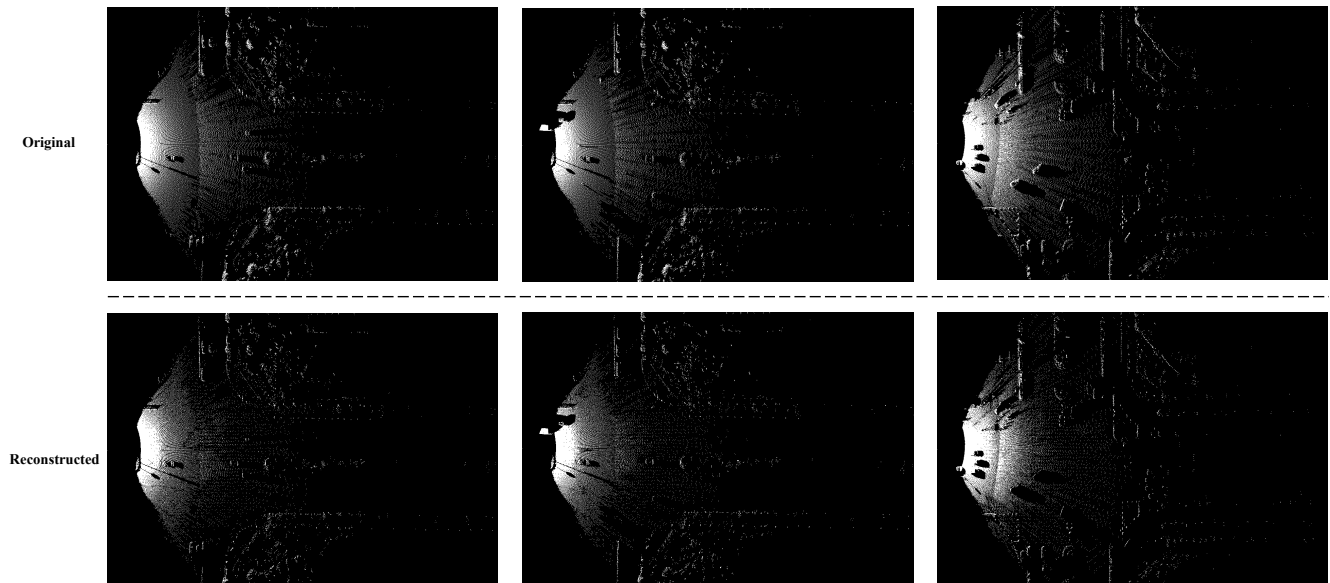


Figure 13. Visualization of BEV representations on the DAIR-V2X dataset. The top row displays the original point cloud BEV maps, and the bottom row shows the reconstructed BEV maps derived from discrete indices. The reconstruction quality demonstrates the strong representation capability and information retention of the DCR module across different domains.

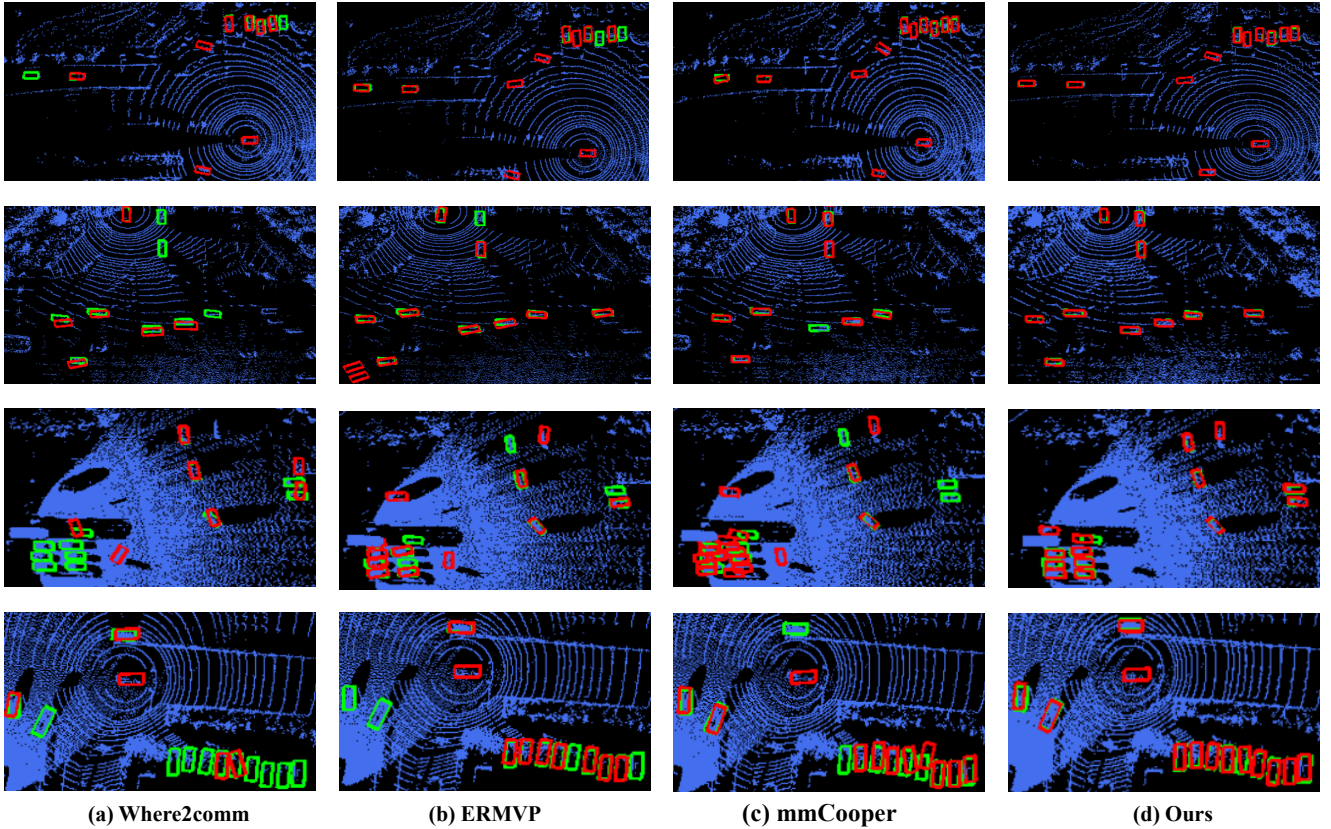


Figure 14. Additional qualitative comparison of detection results on the DAIR-V2X dataset. Green and red bounding boxes denote the ground-truth annotations and the predictions generated by the models, respectively.

Table 9. AP@0.7 under different communication latency (s) on OPV2V and DAIR-V2X.

Method	OPV2V					DAIR-V2X				
	0.0s	0.1s	0.2s	0.3s	0.4s	0.0s	0.1s	0.2s	0.3s	0.4s
Ours	86.81	81.78	80.66	80.70	77.92	56.50	53.10	51.67	51.83	51.63
mmCooper	86.41	78.57	77.44	75.95	75.26	56.06	53.05	50.96	49.86	50.81
ERMVP	80.55	71.42	68.89	68.52	68.31	53.27	49.81	49.68	48.74	48.60
Where2comm	78.47	71.60	65.23	58.73	53.33	52.34	49.74	47.76	45.83	45.25
V2X-ViT	77.88	71.41	66.08	55.71	54.74	46.12	45.69	45.49	44.54	43.99
DiscoNet	77.00	69.20	63.30	57.40	53.20	45.50	45.10	44.60	44.10	43.60
SICP	71.48	68.23	67.81	68.01	67.34	41.72	40.95	40.29	40.08	38.40
When2com	70.82	58.87	43.96	39.90	36.35	39.50	38.24	36.83	35.18	33.72
No Fusion	48.66	48.66	48.66	48.66	48.66	43.57	43.57	43.57	43.57	43.57

Table 10. AP@0.7 under different localization error (m) on OPV2V and DAIR-V2X.

Method	OPV2V					DAIR-V2X				
	0.0 m	0.1 m	0.2 m	0.3 m	0.4 m	0.0 m	0.1 m	0.2 m	0.3 m	0.4 m
Ours	86.81	85.91	85.50	83.68	80.30	56.50	55.68	55.72	50.53	49.46
mmCooper	86.41	84.15	82.35	79.70	76.80	56.06	52.77	51.25	48.17	47.66
ERMVP	80.55	79.07	76.19	75.46	72.78	53.27	51.91	48.66	46.66	45.97
Where2comm	78.47	77.27	75.45	72.14	69.77	52.34	51.05	49.34	47.90	46.96
V2X-ViT	77.88	76.31	75.21	70.77	66.72	46.09	45.21	43.81	42.83	42.53
DiscoNet	77.00	75.80	71.50	66.40	60.50	45.50	45.10	44.30	43.20	41.90
SICP	71.48	68.36	68.30	67.83	67.11	41.72	41.35	40.97	40.58	39.59
When2com	70.82	67.92	64.35	62.48	59.98	39.50	38.06	36.62	35.84	35.03
No Fusion	48.66	48.66	48.66	48.66	48.66	43.57	43.57	43.57	43.57	43.57

Table 11. AP@0.7 under different heading errors ($^{\circ}$) on OPV2V and DAIR-V2X.

Method	OPV2V					DAIR-V2X				
	0.0 $^{\circ}$	0.1 $^{\circ}$	0.2 $^{\circ}$	0.3 $^{\circ}$	0.4 $^{\circ}$	0.0 $^{\circ}$	0.1 $^{\circ}$	0.2 $^{\circ}$	0.3 $^{\circ}$	0.4 $^{\circ}$
Ours	86.81	86.43	85.64	84.33	81.81	56.50	56.37	53.76	52.70	51.34
mmCooper	86.41	84.82	83.18	81.70	79.91	56.06	54.77	53.11	50.17	49.70
ERMVP	80.55	77.07	74.32	72.46	71.23	53.27	52.81	51.38	47.66	48.48
Where2comm	78.47	77.27	75.45	72.14	69.77	52.34	51.75	50.39	49.47	48.76
V2X-ViT	75.88	75.71	75.69	74.77	73.89	46.09	45.81	45.54	45.23	44.77
DiscoNet	77.00	74.38	72.50	68.30	67.54	45.50	44.45	43.38	42.25	41.59
SICP	71.48	69.56	68.37	67.23	67.12	41.72	40.43	41.03	40.16	39.89
When2com	70.82	68.92	67.90	66.48	65.67	39.50	39.06	38.37	37.32	36.90
No Fusion	48.66	48.66	48.66	48.66	48.66	43.57	43.57	43.57	43.57	43.57